Stoichiometry of the $LaFeO_3$ (010) surface determined from first-principles and thermodynamic calculations

Chan-Woo Lee (이 찬우),[1] Rakesh K. Behera,[1] Eric D. Wachsman,[2] Simon R. Phillpot,[1] and Susan B. Sinnott[1,*]

[1]*Department of Materials Science and Engineering, University of Florida, Gainesville, Florida 32611-6400, USA*

[2]*University of Maryland Energy Research Center, University of Maryland, College Park, Maryland 20742, USA*

(Received 29 June 2010; revised manuscript received 26 December 2010; published 11 March 2011)

The phase diagram of $LaFeO_3$ (010) surfaces is developed by *ab initio* thermodynamics. The stabilities of LaO- and FeO_2-terminated surfaces are investigated at temperatures representative of solid oxide fuel cell (SOFC) operating conditions [773, 1073, and 1223 K at $p(O_2) \approx 0.21$ atm]. For LaO-type surfaces, it is predicted that the most stable surface structure is oxidized at all temperatures considered. For FeO_2-type surfaces, the most stable surface structure is predicted to change from oxidized (at 773 K) to stoichiometric (at 1073 and 1223 K). Even though both LaO and FeO_2 surfaces can be oxidized under SOFC operating conditions, the degree of oxidation is much greater for the LaO surface. In addition, as reduced surfaces are predicted to be significantly more unstable than stoichiometric and oxidized terminations at these temperatures and oxygen partial pressures, surface oxygen vacancies are not predicted to form on either the LaO or the FeO_2 terminations. Moreover, at high temperatures [above ~1500 K at $p(O_2) = 0.21$ atm], only FeO_2-type surfaces are predicted to be stable. Importantly, the calculated transition temperatures where surface oxygen stoichiometries are predicted to change are in good agreement with the results of temperature-programmed desorption experiments.

DOI: 10.1103/PhysRevB.83.115418 PACS number(s): 31.15.A−, 88.30.pn, 68.35.Md, 68.47.Gh

I. INTRODUCTION

The oxygen reduction reactions on the surfaces of solid oxide fuel cell (SOFC) cathodes have attracted considerable attention. Candidate materials for the cathodes include ABO_3-type perovskites containing La, Ba, and Sr on the *A* sites and transition metals, such as Mn, Fe, Co, and Ni on the *B* sites. Among these candidates, $LaFeO_3$-based perovskites (LFOs) including $La_{1-x}Sr_xCo_yFe_{1-y}O_{3-\delta}$ have been considered for use as cathode materials in intermediate-temperature SOFCs. The attractiveness of LFOs relies, in part, on the high catalytic activity of oxygen reduction reactions on their surfaces, and their mixed ionic-electronic conducting characteristics, which differ from the behavior of $LaMnO_3$-based perovskites (e.g., $La_{1-x}Sr_xMnO_3$) that are electronic conductors.

As SOFCs operate at relatively high oxygen partial pressures, $p(O_2) \approx 0.21$ atm, and at a wide range of temperatures (T) that vary from 500 to 1000 °C, it is probable that the surface structure of the SOFC cathode is different from its stoichiometric counterpart. Therefore investigating the contribution of environmental parameters to the surface structure of cathode materials is imperative to ultimately understand oxygen reduction reactions in SOFC devices.[1]

Despite the merit of electronic structure calculations to directly compare material stabilities,[2,3] relatively few studies on SOFC cathode materials have been devoted to surface stability as a function of oxygen stoichiometry. For instance, Mastrikov *et al.* showed that the MnO_2 termination with adsorbed oxygen is the most stable form of the (010) surface for cubic $LaMnO_3$ at $p(O_2) \approx 0.21$ atm and $T = 1200$ K, but only MnO_2- and LaO-terminated surfaces with and without adsorbed oxygen atoms were considered.[4] In addition, the stabilization mechanisms due to electron redistribution within LFO (010) surfaces with different surface oxygen stoichiometries were explored by some of us in a previous paper.[5] In particular, it was predicted that oxygen reduction should occur more favorably on the stoichiometric FeO_2 surface than on its stoichiometric counterpart with LaO-type terminations due to the multivalent character of the Fe ion. It was also predicted that the oxidation of the LaO surface should be energetically more favorable than the oxidation of the FeO_2 surface; however, no attempt was made to correlate these stabilization mechanisms to environmental conditions.

The present paper thus characterizes the effects of environment on the surface oxygen stoichiometry of LFO under SOFC operating conditions using a combination of density-functional theory (DFT) and thermodynamics calculations. In this study, the LFO (010) plane is chosen because it has been examined experimentally and theoretically in various other perovskites including $BaTiO_3$, $SrTiO_3$, $LaAlO_3$, and $BaZrO_3$.[6–12]

The rest of this paper is organized as follows: after providing computational details in Sec. II that include specifics of the DFT calculations and thermodynamic model of surface energy calculations, the surface phase diagrams are discussed in Sec. III. In Sec. IV, predictions from the calculated surface phase diagram are compared to the results of temperature-programmed desorption experiments. The conclusions of the paper are provided in Sec. V.

II. COMPUTATIONAL DETAILS

A. Density-functional-theory calculations

The DFT calculations are carried out using the Vienna *Ab-initio* Simulation Package (VASP).[13,14] The spin-polarized generalized gradient approximation (GGA) functional parametrized by Perdew, Burke, and Ernzerhof (PBE) is used to describe the exchange and correlation energies of the electrons. Projector-augmented-wave (PAW) potentials with valence configurations of $5s^25p^65d^16s^2$, $3p^63d^64s^2$, and $2s^22p^4$ are used to describe the La, Fe, and O atoms, respectively. The magnetic moments of the Fe atoms are treated collinearly. Based on convergence tests of the total energy and lattice constant of bulk LFO, plane waves with an

energy cutoff of 600 eV are used to expand the electronic wave functions. $3 \times 3 \times 1$ k-point Monkhorst-Pack meshes are used for integrations over the Brillouin zone of the LFO surface.[15] The ionic relaxation is performed until the Hellmann-Feynman force on each atom is less than 0.01 eV/Å.

Even though DFT calculations with the Hubbard correction (DFT+U) (Ref. 16) are often used in calculating the electronic structures of various bulk oxides,[17,18] there is no general agreement about the validity of DFT+U for predicting the stabilities of oxide surfaces.[19] Therefore this approach is not used in the present paper.

Each surface slab is built symmetrically with a thickness of nine or more atomic layers. The positions of all of the atoms in the system are fully relaxed with the exception of the atoms in the center layer of each slab, which are held fixed.

B. $LaFeO_3$ (010) surface

We construct the 16 stoichiometrically and structurally different (010) surface terminations with a (1×1) surface unit cell: seven surface terminations based on the stoichiometric LaO surface and nine based on the stoichiometric FeO_2 surface (see Table I). In the present paper, only surface oxygen stoichiometry has been varied: this is reasonable, as oxygen is continuously supplied to the surface of SOFC cathodes.

The following nomenclature is used to describe the various surface terminations, and is based on the number of oxygen atoms that are varied in the LaO and FeO_2 topmost layers. The terminations are denoted LaO + xO and FeO_2 + xO, where $\boldsymbol{x}$ describes the number of added or removed O atoms at the surface per LaO or FeO_2 unit. As there are two FeO_2 or LaO units in each layer of the (1×1) surface unit cell, if there is one undercoordinated O atom (O_{low}) on the topmost LaO layer, for example, the corresponding surface termination is described as LaO + $0.5O_{low}$. This nomenclature for describing the surface oxygen stoichiometry is the same as that used by us previously.[5]

Because our focus is to gain a qualitative picture of surface oxygen stoichiometry, the ordering of surface oxygen atoms is not considered in comparing the stabilities of model surfaces. Here, the lateral interactions between surface O_{low} atoms are estimated from previous studies on other oxide surfaces. In particular, Wang and Reuter's DFT results indicate that lateral interactions of adsorbed atomic oxygen on the RuO_2 (110) surface is negligible.[18,20] Additionally, in our work, the energies of the various xO stoichiometries are precise to within $(x + 0.5)$O and $(x - 0.5)$O because of the way in which the stoichiometric gridding was carried out.

TABLE I. Surface terminations of $LaFeO_3$ (010) with a variation of oxygen stoichiometry.

LaO-type	FeO_2-type
	$FeO_2 - 2.0O$
	$FeO_2 - 1.5O$
$LaO - 1.0O$	$FeO_2 - 1.0O$
$LaO - 0.5O$	$FeO_2 - 0.5O$
LaO	FeO_2
$LaO + 0.5O_{low}$	$FeO_2 + 0.5O_{low}$
$LaO + 1.0O_{low}$	$FeO_2 + 1.0O_{low}$
$LaO + 1.5O_{low}$	$FeO_2 + 1.5O_{low}$
$LaO + 2.0O_{low}$	$FeO_2 + 2.0O_{low}$

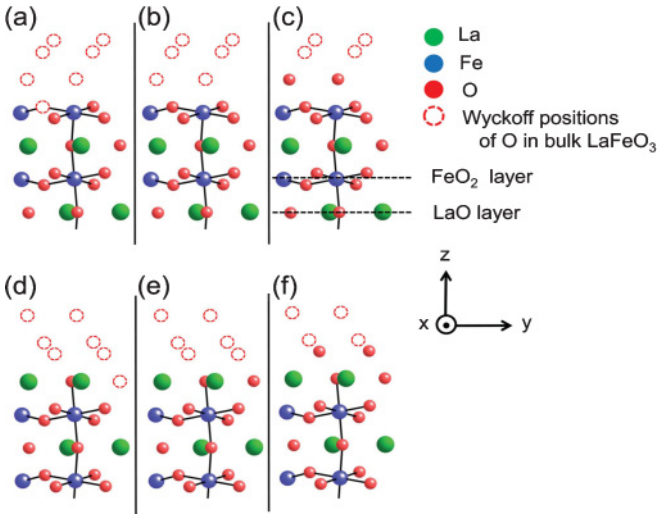

FIG. 1. (Color online) Schematics of FeO_2-type surface terminations: (a) $FeO_2 - 0.5O$, (b) FeO_2, and (c) $FeO_2 + 1.0O_{low}$; LaO-type surface terminations: (d) $LaO - 0.5O$, (e) LaO, and (f) $LaO + 1.0O_{low}$. Dotted circles are Wyckoff positions for O atoms based on bulk $LaFeO_3$ symmetry.

Prior to structural optimization, the O_{low} atoms are placed at the Wyckoff positions of the O atoms in bulk LFO. In all cases the topmost FeO_2 or LaO layer in contact with the vacuum region is designated as the first layer. For surfaces with an overlayer of O_{low} atoms, the layer of O_{low} atoms is designated as layer zero. For convenience, LaO + xO and FeO_2 + xO surface terminations will be simply designated as LaO-type and FeO_2-type surface terminations, respectively. Figures 1(a)–1(c) illustrate the $FeO_2 - 0.5O$, FeO_2, and $FeO_2 + 1.0O_{low}$ surface terminations, while Figs. 1(d)–1(f) show the $LaO - 0.5O$, LaO, and $LaO + 1.0O_{low}$ surface terminations.

C. Thermodynamic model

1. Surface Gibbs free energy and range of allowed chemical potentials

To determine the stable surface oxygen stoichiometry at different environmental variables, the surface Gibbs free energy of each surface termination is calculated. The thermodynamic analysis in this section follows an established framework[8,9,20,21] with the addition of vibrational analysis.

The surface Gibbs free energy for surface termination i, Ω^i is

$$\Omega^i = \frac{1}{2}\left[G^i_{\text{slab}} - \sum_j N^i_j \mu_j\right] = \frac{1}{2}\left[G^i_{\text{slab}} - N^i_{\text{La}}\mu_{\text{La}} - N^i_{\text{Fe}}\mu_{\text{Fe}} - N^i_{\text{O}}\mu_{\text{O}}\right], \quad (1)$$

where G^i_{slab} is the Gibbs free energy of the surface slab i. N^i_j is the number of each type j atom within the slab and μ_j is the chemical potential of each atomic component j in bulk LFO, for j = La, Fe, and O. The chemical potential term, $\sum_j N^i_j \mu_j$ is the Gibbs free energy of the material in the slab if it was reversibly inserted into a materials reservoir.[22] The factor of $\frac{1}{2}$ comes from the use of a symmetric surface slab that contains two identical surface terminations. From Eq. (1), Ω^i is defined as the excess Gibbs free energy due to the presence of the surface. The $\Gamma^i_{m,n}$ term, which is the number of off-stoichiometric atoms of component n with respect to component m in each slab i, is

$$\Gamma^i_{m,n} = \frac{1}{2}\left(N^i_n - N^i_m \frac{N^{\text{bulk}}_n}{N^{\text{bulk}}_m}\right), \tag{2}$$

where the values of $N^{\text{bulk}}_{\text{La}}$, $N^{\text{bulk}}_{\text{Fe}}$, and $N^{\text{bulk}}_{\text{O}}$ are 1, 1, and 3, respectively. Taking Fe as m, Eq. (1) can be combined with Eq. (2) to form

$$\Omega^i = \tfrac{1}{2}\left[G^i_{\text{slab}} - N^i_{\text{Fe}}(\mu_{\text{La}} + \mu_{\text{Fe}} + 3\mu_{\text{O}})\right] - \Gamma^i_{\text{Fe,La}}\mu_{\text{La}} - \Gamma^i_{\text{Fe,O}}\mu_{\text{O}}. \tag{3}$$

The surface Gibbs free energy can be expressed by defining T, $p(O_2)$, and the chemical potentials of either of the cations. In this paper, we choose μ_{La} as one of the variables; choosing μ_{Fe} instead does not change the results. In order to evaluate the surface Gibbs free energy, μ_{Fe} is determined as

$$\mu_{\text{La}} + \mu_{\text{Fe}} + 3\mu_{\text{O}} = \mu_{\text{LaFeO}_3}. \tag{4}$$

This states that the chemical potential of LFO, μ_{LaFeO_3}, is equal to the sum of the chemical potentials of each atomic type in the LFO crystal. As the surface of each slab must be in equilibrium with bulk LFO, μ_{LaFeO_3}, is identical to the Gibbs free energy of bulk LFO:

$$\mu_{\text{LaFeO}_3} = g^{\text{bulk}}_{\text{LaFeO}_3}. \tag{5}$$

By combining with Eqs. (4) and (5), Eq. (3) can be simplified to

$$\Omega^i = \tfrac{1}{2}\left[G^i_{\text{slab}} - N^i_{\text{Fe}} g^{\text{bulk}}_{\text{LaFeO}_3}\right] - \Gamma^i_{\text{Fe,La}}\mu_{\text{La}} - \Gamma^i_{\text{Fe,O}}\mu_{\text{O}}. \tag{6}$$

There are boundary conditions which restrict the physical range of μ_{La} and μ_{O}. First, in order to prevent the spontaneous degradation of LFO surfaces, Ω^i must be positive. Second, since the system does not precipitate into metals and oxides, the following conditions must be satisfied:

$$\mu_{\text{La}} \leqslant g^{\text{bulk}}_{\text{La}}, \tag{7}$$

$$\mu_{\text{Fe}} \leqslant g^{\text{bulk}}_{\text{Fe}}, \tag{8}$$

$$2\mu_{\text{La}} + 3\mu_{\text{O}} \leqslant g^{\text{bulk}}_{\text{La}_2\text{O}_3}, \tag{9}$$

$$\mu_{\text{Fe}} + \mu_{\text{O}} \leqslant g^{\text{bulk}}_{\text{FeO}}, \tag{10}$$

$$2\mu_{\text{Fe}} + 3\mu_{\text{O}} \leqslant g^{\text{bulk}}_{\text{Fe}_2\text{O}_3}, \tag{11}$$

$$3\mu_{\text{Fe}} + 4\mu_{\text{O}} \leqslant g^{\text{bulk}}_{\text{Fe}_3\text{O}_4}. \tag{12}$$

The total energies of the metals and oxides are calculated using their respective atomic structures and magnetic ground states at 0 K; these are given in Table II. The oxygen-rich condition is defined as the point beyond which gaseous O_2 starts to condense on the surface. However, condensed O_2 does not exist SOFC processing conditions (gaseous O_2 condenses to liquid at 90.2 K). This condition provides an upper limit of μ_{O}:

$$\mu_{\text{O}} \leqslant \tfrac{1}{2}E_{\text{O}_2}. \tag{13}$$

Due to the periodic boundary conditions which are applied in our DFT calculations,[23] the distance between an O_2 molecule and its periodic image is 20 Å, which corresponds to an O_2 density that is higher than that of liquid oxygen. Consequently, E_{O_2} in Eq. (13) corresponds to the total energy of condensed O_2 molecules at 0 K without the vibrational contribution (zero-point energy).

Even though the calculated binding energy of O_2 (5.66 eV) is consistent with the results of other DFT calculations with the GGA-PBE functional,[24] it is higher than the experimental binding energy of 5.23 eV.[25] This overestimation in the binding energy is a well-known weakness of DFT. However, this intrinsic error from DFT does not affect our results as $\frac{1}{2}E_{\text{O}_2}$ is well above the μ_{O} range in which we are interested. Nonetheless, calculating accurate total energies of O_2 can be crucial for applications at high $p(O_2)$ and/or low T. Rather than using chemical potentials themselves as variables, we use deviations of chemical potentials from their reference states as variables.[6,8] In particular, instead of μ_{La} and μ_{O}, we use $\Delta\mu_{\text{La}} = \mu_{\text{La}} - E_{\text{La}}$ and $\Delta\mu_{\text{O}} = \mu_{\text{O}} - \frac{1}{2}E_{\text{O}_2}$ as variables with E_{La} and $\frac{1}{2}E_{\text{O}_2}$ as reference states for La and O, respectively.

We explicitly consider the contribution of the vibrational free energy, F^{vib}, to the surface Gibbs free energy and the

TABLE II. Space group, magnetic state, and calculated formation energy of considered secondary phases of bulk $LaFeO_3$.

	Space group	Magnetic state[a]	Formation energy (eV/unit) [deviation from experimental data[b] (%)]
$LaFeO_3$	$Pnma$	AFM	−13.91 [0.52]
La	$P6_3/mmc$	NM	
La_2O_3	$P6_3/mmc$	NM	−18.95 [1.90]
Fe	$Im\bar{3}m$	FM	
FeO	$R\bar{3}m$	AFM	−2.29 [−18.64]
Fe_2O_3	$R\bar{3}c$	AFM	−7.61 [−11.11]
Fe_3O_4	$Fd\bar{3}m$	FiM	−11.33 [−2.46]

[a]NM: nonmagnetic; FM: ferromagnetic; AFM: antiferromagnetic; FiM: ferrimagnetic.
[b]T = 298.15 K.

stability region of bulk LFO. Reuter and Scheffler showed that the vibrational contribution to the surface Gibbs free energy is negligible in the case of RuO_2 (110) surfaces.[20] However, the vibrational effect can be significant when surfaces with similar stabilities are compared, especially when the vibrational contribution includes absolute F^{vib} terms of off-stoichiometric atoms. In particular, the Gibbs free energy g is approximated as total energy E and F^{vib}:

$$g = E + F^{\text{vib}} - TS^{\text{conf}} + pV \approx E + F^{\text{vib}}. \tag{14}$$

Here, the terms $F^{\text{vib}} = E^{\text{vib}} - TS^{\text{vib}}$, p, V, and S^{conf} correspond to vibrational free energy, vibrational energy, temperature, vibrational entropy, pressure, volume, and configurational entropy, respectively. In addition, pV and TS^{conf} are approximated to be zero due to their negligible energetic contributions, as has been done in previous studies.[8,20,26] Thus g in Eq. (14) is simplified to contributions from only E and F^{vib}. This F^{vib} term can be expressed using phonon density of states (DOS) $\sigma(\omega)$ as follows:

$$F^{\text{vib}} = \int d\omega F^{\text{vib}}(T,\omega)\,\sigma(\omega). \tag{15}$$

$F^{\text{vib}}(T,\omega)$ is the vibrational free energy at a given temperature T and vibrational mode ω and is expressed as

$$F^{\text{vib}}(T,\omega) = \tfrac{1}{2}\hbar\boldsymbol{\omega} + \boldsymbol{k}_B T \ln(1 - e^{-\beta\hbar\boldsymbol{\omega}}). \tag{16}$$

Therefore Eqs. (5)–(13) can be rewritten as follows:

$$\Delta\mu_{\text{La}} + \Delta\mu_{\text{Fe}} + 3\Delta\mu_{\text{O}} = \Delta E^{\text{bulk}}_{f,\text{LaFeO}_3} - F^{\text{vib,bulk}}_{\text{LaFeO}_3}, \tag{17}$$

$$\begin{aligned}\Omega^i = &\left[\tfrac{1}{2}\left(E^i_{\text{slab}} - N^i_{\text{Fe}}E^{\text{bulk}}_{\text{LaFeO}_3}\right) - \left(\Gamma^i_{\text{Fe,La}}E_{\text{La}} + \Gamma^i_{\text{Fe,O}}E_{\text{O}}\right)\right]\\ &+ \tfrac{1}{2}\left(F^{\text{vib},i}_{\text{slab}} - N^i_{\text{Fe}}F^{\text{vib,bulk}}_{\text{LaFeO}_3}\right) - \left[\Gamma^i_{\text{Fe,La}}\Delta\mu_{\text{La}} + \Gamma^i_{\text{Fe,O}}\Delta\mu_{\text{O}}\right],\end{aligned} \tag{18}$$

$$\Delta\mu_{\text{La}} \leqslant F^{\text{vib,bulk}}_{\text{La}}, \tag{19}$$

$$\Delta\mu_{\text{La}} + 3\Delta\mu_{\text{O}} \geqslant \Delta E^{\text{bulk}}_{f,\text{LaFeO}_3} + F^{\text{vib,bulk}}_{\text{LaFeO}_3} - F^{\text{vib,bulk}}_{\text{Fe}}, \tag{20}$$

$$2\Delta\mu_{\text{La}} + 3\Delta\mu_{\text{O}} \geqslant \Delta E^{\text{bulk}}_{f,\text{La}_2\text{O}_3} + F^{\text{vib,bulk}}_{\text{La}_2\text{O}_3}, \tag{21}$$

$$\begin{aligned}&\Delta\mu_{\text{La}} + 2\Delta\mu_{\text{O}}\\ &\quad\geqslant \Delta E^{\text{bulk}}_{f,\text{LaFeO}_3} - \Delta E^{\text{bulk}}_{f,\text{FeO}} + F^{\text{vib,bulk}}_{\text{LaFeO}_3} - F^{\text{vib,bulk}}_{\text{FeO}},\end{aligned} \tag{22}$$

$$\begin{aligned}&2\Delta\mu_{\text{La}} + 3\Delta\mu_{\text{O}}\\ &\quad\geqslant 2\Delta E^{\text{bulk}}_{f,\text{LaFeO}_3} - \Delta E^{\text{bulk}}_{f,\text{Fe}_2\text{O}_3} + 2F^{\text{vib,bulk}}_{\text{LaFeO}_3} - F^{\text{vib,bulk}}_{\text{Fe}_2\text{O}_3},\end{aligned} \tag{23}$$

$$\begin{aligned}&3\Delta\mu_{\text{La}} + 5\Delta\mu_{\text{O}}\\ &\quad\geqslant 3\Delta E^{\text{bulk}}_{f,\text{LaFeO}_3} - \Delta E^{\text{bulk}}_{f,\text{Fe}_3\text{O}_4} + 3F^{\text{vib,bulk}}_{\text{LaFeO}_3} - F^{\text{vib,bulk}}_{\text{Fe}_3\text{O}_4},\end{aligned} \tag{24}$$

$$\Delta\mu_{\text{O}} \leqslant 0, \tag{25}$$

where ΔE_f is the formation energy of the corresponding phases that are calculated from DFT (Table II).

In Eq. (18), only the third term $\frac{1}{2}(F^{\text{vib},i}_{\text{slab}} - N^i_{\text{Fe}}F^{\text{vib,bulk}}_{\text{LaFeO}_3})$ describes the vibrational effect on the surface Gibbs free energy, while the first two terms in this equation can be determined from DFT calculations, and $\Delta\mu_{\text{La}}$ and $\Delta\mu_{\text{O}}$ in the last term are variables. For the boundary conditions [Eqs. (17) and (19)–(25)], the formation energies of bulk LFO and other oxides are followed by the F^{vib} terms for relevant bulk materials. The vibrational effect can be as significant in determining the boundary conditions as the surface Gibbs free energy. This is because vibrational contributions in the boundary conditions are not canceled out as a result of different F^{vib} of the corresponding bulk materials.

TABLE III. Vibrational frequencies of La, Fe, the corresponding oxides, and O_{low}.

	Atomic species	Vibrational frequency (cm^{-1})
$LaFeO_3$ (Refs. 28,29)	La	200
	Fe	300
	O	650
Fe (Ref. 29)	Fe	300
FeO (Ref. 30)	Fe and O	480
Fe_2O_3 (Ref. 31)	Fe and O	580
Fe_3O_4 (Ref. 32)	Fe	530
	O	660
La (Ref. 33)	La	73
La_2O_3 (Ref. 34)	La and O	534
O_{low} (Ref. 27)	O	1319

Here, we estimate F^{vib} using the Einstein model and approximate the phonon DOS by one characteristic vibrational frequency (Table III). In calculating F^{vib}, we assume that the vibrational frequencies of the atoms at the surface region (excluding O_{low} atoms) are the same as bulk atoms. Therefore it can be assumed that the vibrational contribution to the surface Gibbs free energy originates from F^{vib} of the off-stoichiometric atoms and the vibrational term in Eq. (18) can be simplified to $\frac{1}{2}\sum_{j=\text{La,O}}\Gamma^i_{\text{Fe},j}F^{\text{vib}}_j$. Additionally, the vibrational frequency of each O_{low} atom is assumed to be independent of surface oxygen stoichiometry, and comes from the calculated frequency of O_2 on the FeO_2 surface of 1319 cm^{-1}.[27]

2. *Chemical potential of oxygen as a function of p(O_2) and T*

Under equilibrium conditions between bulk and gas phases, the chemical potential of oxygen in the LFO bulk is identical to the chemical potential of oxygen in the gas phase:

$$\mu_{\text{O}} = \tfrac{1}{2}\mu^{\text{gas}}_{\text{O}_2}. \tag{26}$$

In addition, under the ideal gas approximation, μ_{O} is directly related to $p(\text{O}_2)$ and T by

$$\mu^{\text{gas}}_{\text{O}_2}(T,p) = \mu^{\text{gas}}_{\text{O}_2}(T,p^0) + kT\ln\left(\frac{p}{p^0}\right), \tag{27}$$

where k is the Boltzmann constant and p^0 is the reference pressure. The $\Delta\mu_{\text{O}}$ can be written as

$$\begin{aligned}\Delta\mu_{\text{O}}(T,p) &= \frac{1}{2}\left[\mu^{\text{gas}}_{\text{O}_2}(T,p^0) - E_{\text{O}_2} + kT\ln\left(\frac{p}{p^0}\right)\right]\\ &= \Delta\mu_{\text{O}}(T,p^0) + \frac{1}{2}kT\ln\left(\frac{p}{p^0}\right).\end{aligned} \tag{28}$$

We determine the $\Delta\mu_{\text{O}}(T,p^0)$ in Eq. (28) using thermodynamic data from the NIST-JANAF thermochemical tables.[35] However, $\Delta\mu_{\text{O}}(T,p^0)[=\frac{1}{2}\Delta G^{\text{gas}}_{\text{O}_2}(T,p^0)]$ from these tables is different from its counterpart in Eq. (28) because the reference T and $p(\text{O}_2)$ of $\frac{1}{2}\Delta G^{\text{gas}}_{\text{O}_2}(T,p^0)$, 298.15 K and 0.98 atm, respectively, are not identical to those of $\Delta\mu_{\text{O}}(T,p^0)(=\frac{1}{2}E_{\text{O}_2})$

from the formalism which is calculated at 0 K. We therefore define

$$\tfrac{1}{2}G^{\mathrm{gas}}_{\mathrm{O}_2}(T^0,p^0) = \tfrac{1}{2}E_{\mathrm{O}_2} + \tfrac{1}{2}\delta G^0_{\mathrm{O}_2} \quad (29)$$

to quantify the difference between these two definitions. This framework follows the approach used by Johnston *et al.*[9]

The Gibbs free energy of the oxygen is expressed in terms of the enthalpy $H^0_{\mathrm{O}_2}(T^0,p^0)$ and entropy $S^0_{\mathrm{O}_2}(T^0,p^0)$ of O_2:

$$\tfrac{1}{2}G^{\mathrm{gas}}_{\mathrm{O}_2}(T^0,p^0) = \tfrac{1}{2}\left[H^0_{\mathrm{O}_2}(T^0,p^0) - T^0 S^0_{\mathrm{O}_2}(T^0,p^0)\right]. \quad (30)$$

In this case, $S^0_{\mathrm{O}_2}(T^0,p^0)$ is directly extracted from the NIST-JANAF tables $[S^0_{\mathrm{O}_2}(T^0,p^0) \approx 2.13\ \mathrm{meV/O_2}]$, while $H^0_{\mathrm{O}_2}(T^0,p^0)$ is determined by the enthalpies of the M_xO_y oxides and M metals (in this case, M = La and Fe), and heats of formation for the oxides. In particular, the enthalpy of an M_xO_y oxide can be written as

$$h^0_{M_x\mathrm{O}_y} = xh^0_M + \frac{y}{2}h^0_{\mathrm{O}_2} + \Delta H^0_{f,M_x\mathrm{O}_y}. \quad (31)$$

Here, the enthalpies of the oxide, $h^0_{M_x\mathrm{O}_y}$, and metal, h^0_M, are determined by E obtained from the DFT calculations, while their corresponding E^{vib} are determined by the Einstein model [Eq. (14)], while formation enthalpy of the oxide, $\Delta H^0_{f,M_x\mathrm{O}_y}$, come from the NIST-JANAF tables[35] (Table I). We use averaged values of $\frac{1}{2}\delta G^0_{\mathrm{O}_2}$ from all the considered oxides ($\frac{1}{2}\delta G^0_{\mathrm{O}_2} = -0.01$ eV with standard deviation of 0.25 eV). This deviation comes, at least in part, from the approximation for vibrational frequencies of the bulk materials. The $\frac{1}{2}\delta G^0_{\mathrm{O}_2}$ term includes enthalpy and entropy contributions with different reference states as well as an error in the O_2 binding energy. In addition, there is an error in the $\frac{1}{2}\delta G^0_{\mathrm{O}_2}$ term related to the addition of electrons to the O-2p orbital when lattice oxygen (O^{2-}) is formed from an O_2 molecule.[9,18] While it has been reported that the $\frac{1}{2}\delta G^0_{\mathrm{O}_2}$ correction is dependent upon the choice of exchange-correlation approximation used in DFT calculations,[36] this effect is not explored here.

III. SURFACE PHASE DIAGRAM

The surface phase diagram in Fig. 2 shows the most stable structure of the LFO (010) surface as a function of $\Delta\mu_{\mathrm{La}}$ and $\Delta\mu_{\mathrm{O}}$. The stability region of bulk LFO, which is indicated by the dotted areas, defines the available range of $\Delta\mu_{\mathrm{La}}$ and $\Delta\mu_{\mathrm{O}}$ for surface energy calculations. In particular, red, brown, and blue dotted regions represent the stability regions of bulk LFO at 773, 1223, and 1500 K at $p(\mathrm{O_2})$ = 0.21 atm, respectively. Outside of the range, spontaneous precipitation of secondary phases including La, Fe, and their oxides is thermodynamically favorable. Hence only the surface phase diagram within the stability region is physically

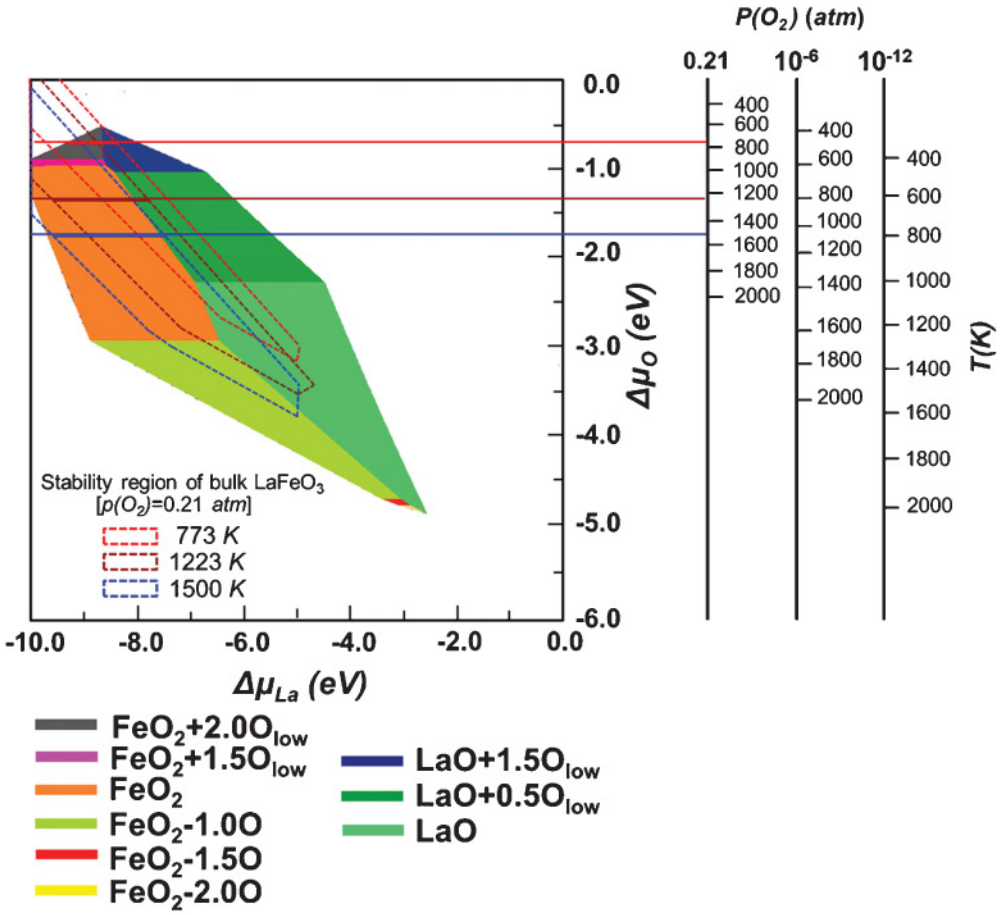

FIG. 2. (Color online) Surface phase diagram of $LaFeO_3$ (010) surfaces. Red, brown, and blue dotted regions indicate stability region of bulk $LaFeO_3$ at 773, 1223, and 1500 K at $p(\mathrm{O_2}) = 0.21$ atm. Similarly, red, brown, and blue parallel lines correspond to $\Delta\mu_{\mathrm{O}}$ at 773, 1223, and 1500 K at $p(\mathrm{O_2}) = 0.21$ atm.

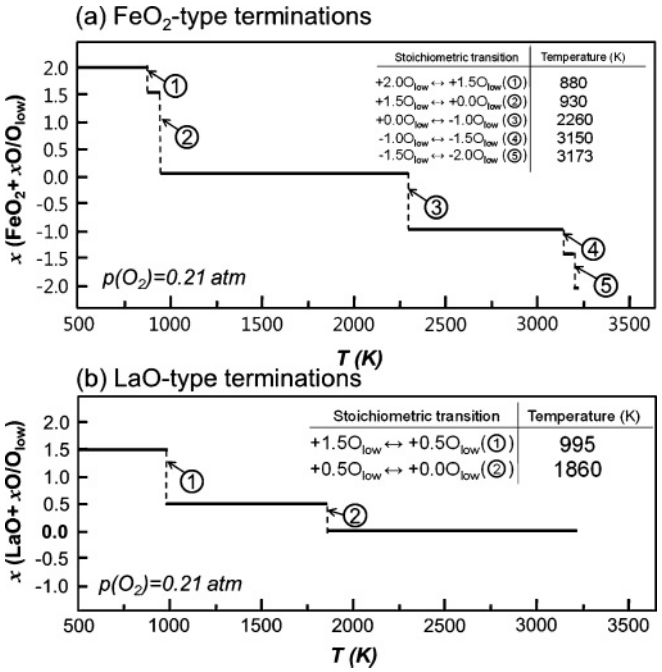

FIG. 3. Line diagrams that show the most stable surface oxygen stoichiometry of (a) FeO_2- and (b) LaO-type surface terminations as a function of temperature. Solid parallel lines indicate the most stable oxygen stoichiometry and dotted vertical lines indicate transition temperatures.

meaningful here. In the y axis, $\Delta\mu_O$ is re-described as functions of $p(O_2)$ (0.21, 10^{-6}, and 10^{-12} atm) and T based on the ideal gas approximation. In this section, only $p(O_2) = 0.21$ atm is considered, and three different temperatures [773 K (≈500 °C), 1073 K (≈800 °C), and 1223 K (≈950 °C)] are chosen to represent different aspects of SOFC operating conditions. Specifically, the temperatures 773 and 1073 K represent the minimum and maximum operating temperatures of intermediate-temperature SOFCs, respectively, while 1223 K is typical of high-temperature SOFCs.

Interestingly, the stability region is predicted to depend strongly on temperature. While Fig. 2 illustrates that both LaO- and FeO_2-type surfaces are possible within operating temperatures of SOFCs, only FeO_2-type surfaces are predicted to be available as temperature increases above ∼1500 K.

One of the important results from the diagram is the temperature associated with several stoichiometric transitions. The transition temperatures of surface oxygen stoichiometry for FeO_2- and LaO- type surfaces are summarized in the form of a line diagram in Fig. 3.

For both FeO_2- and LaO-type surfaces, reduced terminations are not predicted to be the most stable under SOFC operating conditions, which is not surprising given their relatively high oxygen partial pressures and temperatures. In particular, no reduced LaO-type surfaces are predicted to have preferred stability within the surface phase diagram. In contrast, some reduced FeO_2 surfaces are predicted to be stable within the surface phase diagram, but only at temperatures above 2260 K, or much higher than SOFC operating temperatures.

Consequently, under SOFC operating conditions, for FeO_2-type surfaces, the most stable surface structure changes from $FeO_2 + 2.0O_{low}$ (at 773 K) to stoichiometric FeO_2 (at 1073 and 1223 K). For LaO-type surfaces, the oxidized termination is always the most stable ($LaO + 1.5O_{low}$ at 773 K, to $LaO + 0.5O_{low}$ at 1073 and 1223 K).

As discussed above, the atomic vibrational contribution is approximated by one characteristic frequency. However, actual vibrational behavior is more complex and the vibrational mode of surface atoms might be influenced by electronic redistribution at the surface region. It is thus important to investigate how the change in vibrational mode modifies the surface phase diagrams. We therefore recalculated the surface phase diagram with ±20% variations of the characteristic vibrational frequencies of La and O. The stoichiometric order as a function of $\Delta\mu_O$ (or T) is not altered by the variation of frequencies. However, the variation modifies the temperatures for predicted stoichiometric transitions by −40 K (with the −20% variation) and +100 K (with the +20% variation). These are therefore taken as the error range associated with each predicted transition temperature. Additionally, the boundaries between LaO- and FeO_2-type terminations shift by a maximum of 0.12 eV as the vibrational frequencies vary.

Figure 4 illustrates the surface Gibbs free energies of FeO_2- and LaO-type surfaces at fixed $\Delta\mu_O$, with $\Delta\mu_{La}$ and the surface Gibbs free energy Ω as variables. Figures 4(a) and 4(c) can be considered to be cross sections along the top two parallel lines in Fig. 2.

Here, it is assumed that the error involved in comparing stabilities of stoichiometrically different surfaces only comes from the cohesive energy of the nonstoichiometric atoms. Specifically, we set ±0.28 eV as the error range for surface Gibbs free energies. This is the reported error associated with atomization and cohesive energies calculated with the GGA-PBE functional[37] and is more significant than other sources of error, such as cutoff energy and k-point sampling in our calculations.

At 773 K, relative stabilities of $FeO_2 + 2.0O_{low}$ and $FeO_2 + 1.5O_{low}$ surfaces are not distinct as their energy difference (0.19 eV) is less than the error range. On the contrary, the energy difference between the most stable $FeO_2 + 2.0O_{low}$ and stoichiometric and reduced FeO_2-type surfaces ($x \leqslant 0.0$) is larger than 1.0 eV, which indicates that only highly oxidized FeO_2-type surfaces are favorable at 773 K. For LaO-type surfaces, only the $LaO + 1.5O_{low}$ termination is predicted to be available. The most stable $LaO + 1.5O_{low}$ and second-most stable $LaO + 2.0O_{low}$ terminations have an energy difference of 0.4 eV. Additionally, the energy difference between the most stable $LaO + 1.5O_{low}$ and stoichiometric LaO is 2.4 eV; the difference between the $LaO + 1.5O_{low}$ and reduced LaO surfaces is more than 7.3 eV.

At 1073 K, it is not clear which surface among FeO_2, $FeO_2 + 0.5O_{low}$, and $FeO_2 + 1.0O_{low}$ will exist as the differences in their energies (0.15 eV for FeO_2 and $FeO_2 + 0.5O_{low}$ and 0.27 eV for FeO_2 and $FeO_2 + 1.0O_{low}$) are smaller than the uncertainty range. In contrast, other highly oxidized and reduced FeO_2-type surfaces are predicted to be absent. For LaO-type surfaces, $LaO + 0.5O_{low}$, $LaO + 1.0O_{low}$, and $LaO + 1.5O_{low}$ have similar stabilities (energy difference between $LaO + 0.5O_{low}$ and $LaO + 1.0O_{low}$ is 0.2 eV). Other

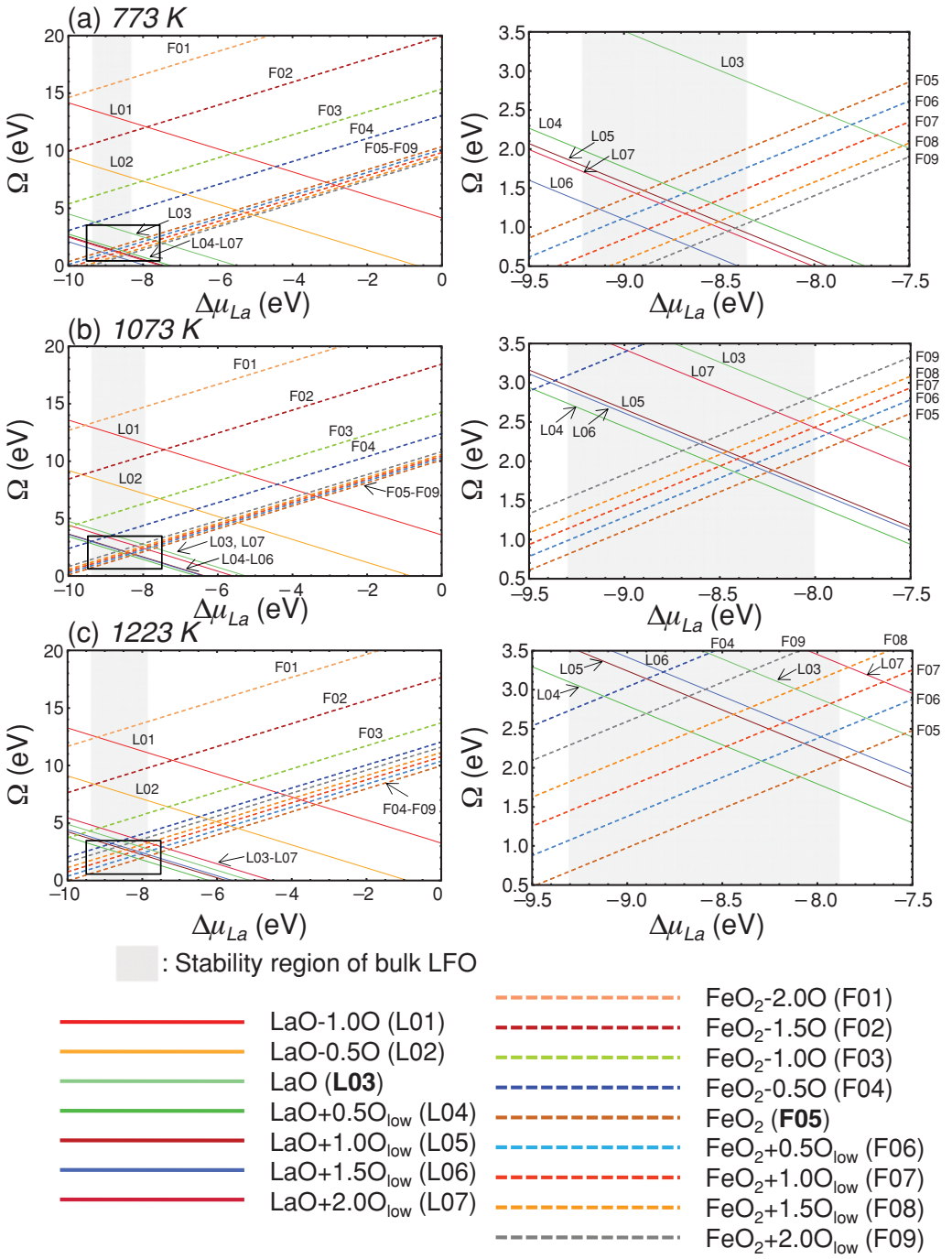

FIG. 4. (Color online) Surface phase diagram at (a) 773 K, (b) 1073 K, and (c) 1223 K with $p(O_2) = 0.21$ atm. The gray highlighted regions in (a), (b), and (c) represent stability region of bulk $LaFeO_3$. The right-hand-side figures for (a), (b), and (c) illustrate the magnified view of the rectangular sections shown in the left-hand-side figures.

LaO-type surfaces ($x \leqslant 0.0$) will not be present at 1073 K as their energies are much larger than those of the favorable surfaces.

At 1223 K, because there is a significant energy difference between the most stable FeO_2 and other less stable FeO_2-type surfaces (>0.4 eV), only the FeO_2 surface should be present. Among the LaO-type surfaces, the $LaO + 0.5O_{low}$ surface should be observed because it is significantly more stable than other LaO-type terminations (>0.4 eV). For both LaO- and FeO_2-type terminations, the energies of the reduced surfaces approach those of the oxidized surfaces as the temperature is increased. However, because of the relatively high oxygen partial pressures, this stabilization is not sufficient to make the reduced surfaces the most stable. Thus surface oxygen vacancies are not predicted to form on either LaO- or FeO_2-type surfaces within this temperature range at this oxygen partial pressure. The surface oxygen stoichiometry predicted here for the FeO_2 (010) is not the same as that predicted by Lee *et al.*,[36] but both sets of calculations predicted low surface oxygen coverage at high temperatures. The variation

of vibrational frequencies can change the energy difference between various surfaces, but this does not alter the predictions regarding available surfaces at each temperature.

IV. RELATION TO EXPERIMENTAL RESULTS

It is interesting to see to what extent we can validate our surface phase diagram against results from temperature-programmed desorption (TPD) and temperature-programmed reduction (TPR) experiments.[38–43] Even though the kinetic factors in the TPD and TPR results were not considered during the development of our surface phase diagrams, it is reasonable to expect that the desorption peaks of the so-called α- and β-oxygen atoms,[41,44,45] which are ascribed to adsorbed (O_{low}) and lattice oxygen atoms, respectively, will correlate with the change in surface oxygen stoichiometry in the diagram. Here, lattice oxygen implies the oxygen atoms in the first layer or subsurface layers. Therefore we compare the temperatures where the surface oxygen stoichiometry is predicted to change with the oxygen desorption trend reported from experiments.

Even though most experiments are performed at high vacuum conditions (10^{-6} to 10^{-12} atm), the $p(O_2)$ in each experiment is slightly different. Because the T corresponding to a specific $\Delta\mu_O$ varies with $p(O_2)$, predicted transition temperatures for $LaO + 1.5O_{low} \leftrightarrow LaO + 0.5O_{low}$, $FeO_2 + 2.0O_{low} \leftrightarrow FeO_2 + 1.5O_{low}$, and $FeO_2 + 1.5O_{low} \leftrightarrow FeO_2$, which are available stoichiometric transitions within the stability of bulk LFO, have a range of 409–591 K under high vacuum conditions (see Fig. 2).

Considering lattice oxygen atoms, Fig. 2 predicts that no surface oxygen vacancies should form until 1251 K. Also, reduced surfaces cannot be the most favorable within the stability of bulk LFO, because there is no overlap between them and the bulk LFO region. This is consistent with the TPD and TPR results, most of which show no desorption peak for β oxygen up to the highest temperatures probed (1273 K).[38–43,46] Instead of surface oxygen vacancies, secondary phases were observed at 850–1250 K, which is also consistent with our predictions.[40,46]

For adsorbed oxygen atoms (O_{low}), the TPD and TPR experiments on LFO generally show two different trends based on the calcination temperature of the ceramic. In the case of LFO calcined below 923 K, desorption for α oxygen was clearly observed. In particular, Tascón *et al*. observed oxygen desorption at 600–850 K at a calcination temperature of 923 K.[40] Similarly, Kim *et al*. detected oxygen desorption from 573 K (there was a significant peak around 973 K) after calcination at 973 K.[38] Finally, Wachowski *et al*. reported two desorption steps at 520–580 K and 720–870 K, respectively, when LFO was calcined at 773 K.[46] In contrast, at a high calcination temperature of 1123 K, most of the experiments reported no desorption peak of α oxygen,[41–43] even though weak peaks below 773 K were observed by Nitadori *et al*.[39] For convenience, in the following discussion, temperatures of 973 K or less will be defined as "low calcination temperatures" and those at 1123 K or higher will be defined as "high calcination temperatures."

The predicted transition temperature range of 409–591 K from the surface phase diagram illustrated in Fig. 2 agrees well with TPD results for samples processed at low calcination temperatures.[38,40,46] The effect of calcination temperature on the desorption trend of adsorbed oxygen O_{low} can be interpreted as the relative stability of LaO- to FeO_2-type surfaces as a function of temperature. In particular, it is predicted from Fig. 2 that FeO_2-type surfaces become more stable than LaO-type terminations above 1500 K. The discrepancy between predicted temperature and the minimum of the high calcination temperatures [i.e., the minimum of the high calcination temperatures (1123 K) is lower than 1500 K] may originate from our approximations on phonon frequencies and surface structures.

Considering that the degree of oxidation is weaker at FeO_2-type terminations than at LaO-type terminations, at high calcination temperatures LFO surfaces that only contain FeO_2-type terminations will experience little desorption of O_{low}. However, for low calcination temperatures, both LaO- and FeO_2-type surfaces are available and a relatively strong desorption peak will be detected. This can also explain the experimental result that the oxidative nonstoichiometry of LFO decreases with increasing calcination temperature.[47]

V. CONCLUSIONS

Our purpose has been to develop the phase diagram of LFO (010) surfaces for varying oxygen stoichiometries. This paper has shown that the contribution of the chemical potentials is significant in the determination of surface stability. Also, the calculated surface phase diagram is consistent with results from TPD and TPR experiments.

The surface phase diagrams lead us to conclude that oxidized surface terminations must be considered to understand oxygen reduction reactions, especially for the research of cathode materials for intermediate temperature SOFCs. Also, the instability of the reduced surfaces with respect to stoichiometric terminations at SOFC operating conditions emphasizes the role of extrinsic defects including Sr and Co in increasing the concentration of surface oxygen vacancies of LFO surfaces.

The dominance of FeO_2-type surfaces at high temperatures (>1500 K) indicates the importance of thermal treatments, such as calcination, for controlling surface structure and the corresponding catalytic activity of LFO and related materials. The surface phase diagram calculated here will serve as a platform for better understanding oxygen reduction reactions at SOFC cathode materials.

ACKNOWLEDGMENTS

We acknowledge the University of Florida High-Performance Computing Center http://hpc.ufl.edu and EMSL, a national scientific user facility sponsored by the Department of Energy's Office (DOE) of Biological and Environmental Research and located at Pacific Northwest National Laboratory, for providing computational resources for performing some of the calculations reported in this paper. C.-W.L. thanks Dongjo Oh, Eric Armstrong, Alex Chernatinskiy, and Eric Lambers (UF) for fruitful discussions. This work was supported by the US Department of Energy High Temperature Electrochemistry Center at the University of Florida, Contract No. DE-AC05-76RL01830.

*ssinn@mse.ufl.edu

[1] N. Sakai, K. Yamaji, T. Horita, Y. P. Xiong, H. Kishimoto, M. E. Brito, and H. Yokokawa, Solid State Ionics **176**, 2327 (2005).

[2] J. He, R. K. Behera, M. W. Finnis, X. Li, E. C. Dickey, S. R. Phillpot, and S. B. Sinnott, Acta Mater. **55**, 4325 (2007).

[3] H. Xu, D. Lee, J. He, S. B. Sinnott, V. Gopalan, V. Dierolf, and S. R. Phillpot, Phys. Rev. B **78**, 174103 (2008).

[4] Y. A. Mastrikov, R. Merkle, E. Heifets, E. A. Kotomin, and J. Maier, J. Phys. Chem. B **114**, 3017 (2010).

[5] C.-W. Lee, R. K. Behera, S. Okamoto, R. Devanathan, E. D. Wachsman, S. R. Phillpot, and S. B. Sinnott, J. Am. Ceram. Soc. (to be published).

[6] F. I. Bottin, F. Finocchi, and C. Noguera, Phys. Rev. B **68**, 035418 (2003).

[7] R. I. Eglitis and D. Vanderbilt, Phys. Rev. B **76**, 155439 (2007).

[8] E. Heifets, J. Ho, and B. Merinov, Phys. Rev. B **75**, 155431 (2007).

[9] K. Johnston, M. R. Castell, A. T. Paxton, and M. W. Finnis, Phys. Rev. B **70**, 085415 (2004).

[10] H. Kawanowa, H. Ozawa, M. Ohtsuki, Y. Gotoh, and R. Souda, Surf. Sci. **506**, 87 (2002).

[11] C. H. Lanier, J. M. Rondinelli, B. Deng, R. Kilaas, K. R. Poeppelmeier, and L. D. Marks, Phys. Rev. Lett. **98**, 086102 (2007).

[12] J. L. Wohlwend, R. K. Behera, I. Jang, S. R. Phillpot, and S. B. Sinnott, Surf. Sci. **603**, 873 (2009).

[13] G. Kresse and J. Furthmüller, Phys. Rev. B **54**, 11169 (1996).

[14] G. Kresse and D. Joubert, Phys. Rev. B **59**, 1758 (1999).

[15] H. J. Monkhorst and J. D. Pack, Phys. Rev. B **13**, 5188 (1976).

[16] V. I. Anisimov, F. Aryasetiawan, and A. I. Lichtenstein, J. Phys.: Condens. Matter **9**, 767 (1997).

[17] D. D. Cuong, B. Lee, K. M. Choi, H.-S. Ahn, S. Han, and J. Lee, Phys. Rev. Lett. **98**, 115503 (2007).

[18] L. Wang, T. Maxisch, and G. Ceder, Phys. Rev. B **73**, 195107 (2006).

[19] A. Barbier, A. Stierle, N. Kasper, M. J. Guittet, and J. Jupille, Phys. Rev. B **75**, 233406 (2007).

[20] K. Reuter and M. Scheffler, Phys. Rev. B **65**, 035406 (2001).

[21] S. Piskunov, E. Heifets, T. Jacob, E. A. Kotomin, D. E. Ellis, and E. Spohr, Phys. Rev. B **78**, 121406 (2008).

[22] J. W. Cahn, in *Interfacial Segregation*, edited by W. J. Johnson and J. M. Blakely (ASM, Metals Park, OH, 1973), p. 3.

[23] M. C. Payne, M. P. Teter, D. C. Allan, T. A. Arias, and J. D. Joannopoulos, Rev. Mod. Phys. **64**, 1045 (1992).

[24] P. Giannozzi, R. Car, and G. Scoles, J. Chem. Phys. **118**, 1003 (2003).

[25] J. A. Pople, M. Head-Gordon, D. J. Fox, K. Raghavachari, and L. A. Curtiss, J. Chem. Phys. **90**, 5622 (1989).

[26] J. Rogal, K. Reuter, and M. Scheffler, Phys. Rev. B **69**, 075421 (2004).

[27] X. Liu, J. Hu, B. Cheng, H. Qin, M. Zhao, and C. Yang, Sens. Actuators B **139**, 520 (2009).

[28] J. Andreasson, J. Holmlund, R. Rauer, M. Kall, L. Borjesson, C. S. Knee, A. K. Eriksson, Sten-G. Eriksson, M. Rubhausen, and R. P. Chaudhury, Phys. Rev. B **78**, 235103 (2008).

[29] G. Lucas and R. Schäblin, Nucl. Instrum. Methods. Phys. Res. B **267**, 3009 (2009).

[30] V. V. Struzhkin *et al.*, Phys. Rev. Lett. **87**, 255501 (2001).

[31] C. J. Serna *et al.*, J. Phys. C **20**, 473 (1987).

[32] N. S. Olga and L. Peter, J. Chem. Phys. **119**, 6100 (2003).

[33] B. A. Oli and J. S. Ononiwu, Physica B + C **138**, 323 (1986).

[34] G. Scarel, A. Debernardi, D. Tsoutsou, S. Spiga, S. C. Capelli, L. Lamagna, S. N. Volkos, M. Alia, and M. Fanciulli, Appl. Phys. Lett. **91**, 102901 (2007).

[35] *NIST-JANAF Thermochemical Tables*, 4th ed., edited by M. W. Chase (American Chemical Society, Washington, DC, 1998).

[36] Y.-L. Lee, J. Kleis, J. Rossmeisl, and D. Morgan, Phys. Rev. B **80**, 224101 (2009).

[37] J. J. Mortensen, K. Kaasbjerg, S. L. Frederiksen, J. K. Nørskov, J. P. Sethna, and K. W. Jacobsen, Phys. Rev. Lett. **95**, 216401 (2005).

[38] K. S. Kim, S. B. Kim, W. J. Choi, T. O. Kim, and H. S. Hahm, J. Ind. Eng. Chem. **7**, 110 (2001).

[39] T. Nitadori and M. Misono, J. Catal. **93**, 459 (1985).

[40] Juan M. D. Tascón, J. L. G. Fierro, and L. G. Tejuca, J. Chem. Soc. Faraday Trans. **1**, 2399 (1985).

[41] Y. Teraoka, M. Yoshimatsu, N. Yamazoe, and T. Seiyama, Chem. Lett. **13**, 893 (1984).

[42] Y. Teraoka, H.-M. Zhang, and N. Yamazoe, Chem. Lett. **14**, 1367 (1985).

[43] Y. Yokoi and H. Uchida, Catal. Today **42**, 167 (1998).

[44] H. Yokokawa, T. Horita, N. Sakai, K. Yamaji, M. E. Brito, Y. P. Xiong, and H. Kishimoto, Solid State Ionics **177**, 3193 (2006).

[45] S. Kaliaguine, A. Van Neste, V. Szabo, J. E. Gallot, M. Bassir, and R. Muzychuk, Appl. Catal. A **209**, 345 (2001).

[46] L. Wachowski, S. Zielinski, and A. Burewicz, Acta Chim. Acad. Sci. Hung. **106**, 217 (1981).

[47] R. J. H. Voorhoeve, J. P. Remeika, and L. E. Trimble, Ann. NY Acad. Sci. **272**, 3 (1976).